Acta Mechanica 145, 1 – 18 (2000)

ACTA MECHANICA


# Transient wave propagation in a one-dimensional poroelastic column

**M. Schanz,** Braunschweig, Germany and **A. H.-D. Cheng,** Newark, DE

(Received January 12, 2000; revised March 29, 2000)

**Summary.** Biot's theory of porous media governs the wave propagation in a porous, elastic solid infiltrated with fluid. In this theory, a second compressional wave, known as the slow wave, has been identified. In this paper, Biot's theory is applied to a one-dimensional continuum. Despite the simplicity of the geometry, an exact solution of the full model, and a detailed analysis of the phenomenon, so far have not been achieved. In the present approach, an analytical solution in the Laplace transform domain is obtained showing clearly two compressional waves. For the special case of an inviscid fluid, a closed form exact solution in time domain is obtained using an analytical inverse Laplace transform. For the general case of a viscous fluid, solution in time domain is evaluated using the Convolution Quadrature Method of Lubich. Of all the inverse methods previously investigated, it seems that only the method of Lubich is efficient and stable enough to handle the highly transient cases such as impact and step loadings. Using properties of three widely different real materials, the wave propagating behavior, in terms of stress, pore pressure, displacement, and flux, are examined. Of most interest is the identification of second compressional wave and its sensitivity of material parameters.

## 1 Introduction

For a wide range of fluid infiltrated materials, such as water saturated soils, oil impregnated rocks, or air filled foams, the elastic theory is a crude approximation for investigating wave propagation in such media. Due to their porosity, a different theory is necessary. A theory of porous materials containing a viscous fluid was presented by Biot [1]. This has been generally attributed as the starting point of the theory of Poroelasticity. In the following years Biot extended his theory to anisotropic case [2] and also to poroviscoelasticity [3]. The dynamic extension was done in two papers, one for low frequency range [4] and the other for high frequency range [5]. Among the significant findings was the identification of three waves for a three-dimensional continuum, two compressional waves and one shear wave. These extra compressional wave, known as the slow wave, has been experimentally confirmed [6].

Another approach to describe the dynamic behavior of porous media, known as the "Theory of Porous Media" [7], is based on the theory of mixtures and derived from the well known methods of continuum mechanics. It has been demonstrated that under small deformations, and some other restrictions, this and Biot's theory lead to the same governing equations [8]. Although Biot's theory is more based on physical intuition, it has the widest acceptance in geophysics and geomechanics.

Independent of which formulation one chooses, the governing equations consist of a system of coupled partial differential equations. To find a close form exact solution for the general material case, even in a simple one-dimensional geometry, has so far not been successful.

Some analytical solutions for one-dimensional (1-d) problems have been found. For example, Grag et al. [9] examined the response of an infinitely long fluid saturated soil column subjected to a Heaviside step function velocity boundary condition at one end. There, Biot's theory was used and a closed form solution was obtained only for the limiting cases of zero and infinite fluid drag. Grag's solution in Laplace transform with a subsequent numerical inversion led to solution of the general material case [10], and was compared to a 1-d Finite Element solution [11]. A solution in frequency domain of a finite 1-d column loaded at the top by total stress and pore pressure was presented in Cheng et al. [12] for comparison with a boundary element solution. Based on the Theory of Porous Media an analytical 1-d solution for an infinitely long column was deduced for incompressible constituents [13]. Finally, for an even more general material case of a partially saturated dual-porosity medium, a 1-d solution in Laplace domain is available from Beskos et al. [14].

It is of interest to observe that of all the prior theoretical investigations of one-dimensional wave propagation, none seems to have examined the problem of impact or step loading and produced the dynamic wave behavior. For loadings that are sinusoidal, similar wave forms are expected. For an impact or step loading in a finite length column, we expect a clear passage of wave form and its subsequent multiple reflections. Of the two impact or step loading solutions reported in the literature [14], [13], only monotonic decay was observed. This could be caused by the use of an extremely dissipative material or the inaccuracy in the numerical inversion algorithm. Since measurements based on pore pressure response conducted in laboratory using real materials typically exhibit these dynamic wave forms, it is of interest to demonstrate such behavior in theoretical solution.

We also notice that none of the prior theoretical analyses using different types of boundary conditions has clearly shown the passage of slow wave. This is not to say that the prior solutions were not correct. This says that the material properties, the boundary conditions, and the column geometry chosen, and the quantities monitored, may not be suitable for the clear detection of slow wave. Since the slow wave differentiates a Biot poroelastic material from an elastic material, it is of interest to use the analytical tool for such an observation.

In the present work, the solution of a finite 1-d column with different types of boundary conditions is deduced based on Biot's theory. This solution is obtained from the frequency domain solution [12], but converted to the Laplace transform domain to find an analytical solution with arbitrary loading history, which involves a convolutional integral. Similar to prior solutions, a numerical technique is needed to find solution in time domain.

This convolution integral is numerically evaluated by the so-called "Convolution Quadrature Method" proposed by Lubich [15]. The weights of this quadrature formula are determined from the Laplace transformed impulse response function and a linear multistep method. In this method, no solution in time domain of the original problem is necessary. Through a series of stringent tests that includes a comparison with the highly acclaimed Dubner-Abate-Durbin-Crump method [14], [16], [17], [18], [19], our experience indicates that the Lubich method is one of the most robust in performing the inversion of wave-like functions that involves a significant number of cycles resulting from impact loading. This method has been, among other applications, successfully applied to a time domain formulation of the boundary element method [20].

Despite our confidence in the Lubich method, it is necessary to compare the solution based on numerical inversion with the direct time domain solution. This is achieved via a special case involving vanishing fluid resistance. This solution is without dissipation and is the most dynamic in nature. An analytical Laplace inversion is possible and closed form solution

in the time domain is presented. The Lubich method is tested against the time domain solution and has produced favorable comparison.

The Lubich method is then used to obtain solution in the time domain for the general case. A number of problems that involve a combination of impulse and step loadings with total stress, pore pressure, and displacement conditions, are examined. Three materials, a rock, a soil, and a seabottom sediment, representing a wide range of material properties, are investigated. The column response to dynamic loading can be examined in terms of stress, pore pressure, solid displacement, and fluid flux. In many of the cases, we clearly observe the creation and propagation of the second compressional wave. With the present solution capability, we have offered a powerful tool that can simulate a column response under a wide range of transient loading conditions.

## 2 Governing equations

Following Biot's approach to model the behavior of porous media, the constitutive equations can be expressed as [1]

$$\sigma_{ij} = G\varepsilon_{ij} + \left(K - \frac{2}{3}G\right)\varepsilon_{kk}\delta_{ij} - \alpha\delta_{ij}p\,, \tag{1.1}$$

$$\zeta = \alpha\varepsilon_{kk} + \frac{\phi^2}{R}p\,, \tag{1.2}$$

in which $\sigma_{ij}$ denotes the total stress, $p$ the pore pressure, $\varepsilon_{ij}$ the strain of the solid frame, $\zeta$ the variation of fluid volume per unit reference volume, and $\delta_{ij}$ the Kronecker delta. In the above, the sign conventions for stress and strain follow that of elasticity, namely, tensile stress and strain is denoted positive. The Latin indices takes the values 1, 2, 3 or 1, 2 in 3-d or 2-d cases, respectively, where summation convention is implied over repeated indices. The bulk material is defined by the material constants shear modulus $G$ and the drained bulk compression modulus $K$. The porosity $\phi$, Biot's effective stress coefficient $\alpha$ and $R$ complete the set of material parameters. The last two mentioned parameters can be calculated taking some micro mechanical considerations into account by [21]

$$\alpha = 1 - \frac{K}{K_s} \tag{2}$$

and

$$R = \frac{\phi^2 K_f {K_s}^2}{K_f(K_s - K) + \phi K_s(K_s - K_f)}\,, \tag{3}$$

where $K_s$ denotes the compression modulus of the solid grains and $K_f$ the compression modulus of the fluid.

Now, the governing equations are completed by the dynamic equilibrium

$$\sigma_{ij,j} + F_i = \varrho\frac{\partial^2 u_i}{\partial t^2} + \phi\varrho_f\frac{\partial^2 v_i}{\partial t^2}\,, \tag{4}$$

and the continuity equation

$$\frac{\partial\zeta}{\partial t} + q_{i,i} = 0\,, \tag{5}$$

where the bulk density $\varrho = \varrho_s(1-\phi) + \phi\varrho_f$ with the densities of the solid $\varrho_s$ and the fluid $\varrho_f$ is used. As well the displacements of the solid are denoted by $u_i$ and the relative fluid to solid displacements by $v_i$. In Eqs. (4) and (5) and in the following, vanishing initial conditions for all variables are assumed. $F_i$ are the bulk body forces which are neglected in the following, and $q_i = \phi(\partial y_i)/\partial t$ denotes the specific flux of the fluid. Finally, the derivative with respect to the spatial variable $x_i$ is abbreviated by $(),_i$. The fluid is modeled with Darcy's law

$$q_i = -\varkappa\left(p_{,i} + \varrho_f \frac{\partial^2 u_i}{\partial t^2} + \frac{\varrho_a + \phi\varrho_f}{\phi}\frac{\partial^2 v_i}{\partial t^2}\right), \tag{6}$$

where $\varkappa$ denotes the permeability and $\varrho_a$ the apparent mass density. For simplicity, the apparent mass density $\varrho_a$ is assumed to be frequency independent as $\varrho_a = 0.66\,\phi\varrho_f$ [22].

As shown in [23], it is sufficient to use the solid displacements and the pore pressure as basic variables to describe a poroelastic continuum. Therefore, the above equations are reduced to these four unknowns. To do this, Eqs. (4), (5) and (6) are transformed to Laplace domain. Taking a linear strain-displacement relation into account $\varepsilon_{ij} = 1/2(u_{i,j} + u_{j,i})$, i.e., small deformation gradients are assumed, the final set of differential equations for the displacements $\hat{u}_i$ and the pore pressure $\hat{p}$ are achieved

$$G\hat{u}_{i,jj} + \left[K + \frac{1}{3}G\right]\hat{u}_{j,ij} - (\alpha-\beta)\,\hat{p}_{,i} - s^2(\varrho - \beta\varrho_f)\,\hat{u}_i = 0 \tag{7}$$

$$\frac{\beta}{s\varrho_f}\hat{p}_{,ii} - \frac{\phi^2 s}{R}\,\hat{p} - (\alpha-\beta)\,s\hat{u}_{i,i} = 0\,, \tag{8}$$

which the abbreviation

$$\beta = \frac{\phi^2 s\varkappa\varrho_f}{\phi^2 + s\varkappa(\varrho_a + \phi\varrho_f)}\,, \tag{9}$$

and $\mathscr{L}\{f(t)\} = \hat{f}(s)$ denotes the Laplace transform, with the complex Laplace variable $s$. With this set of equations the behavior of a poroelastic continuum is completely given.

## 3 Analytical solution

A one-dimensional column of length $\ell$ as sketched in Fig. 1 is considered. It is assumed that the side walls and the bottom are rigid, frictionless, and impermeable. Hence, the displacements normal to the surface are blocked and the column is otherwise free to slide parallel to the wall. At the top, the stress $\sigma_y$ and the pressure $p$ are prescribed. Due to these restrictions only the displacement $u_y$ and the pore pressure $p$ remain as degrees of freedom. This one-dimensional example can be used to study the influence of poroelastic parameters on wave propagation, or it can be seen as an approximation of a poroelastic half-space by setting the layer depth $\ell$ large. Here, we are particular interested in observing the interplay of the two compressional waves.

For this, the governing set of differential equations (7) and (8) is reduced to two scalar coupled ordinary differential equations:

$$E\hat{u}_{y,yy} - (\alpha-\beta)\hat{p}_{,y} - s^2(\varrho - \beta\varrho_f)\,\hat{u}_y = 0\,, \tag{10}$$

$$\frac{\beta}{s\varrho_f}\,\hat{p}_{,yy} - \frac{\phi^2 s}{R}\,\hat{p} - (\alpha-\beta)\,s\hat{u}_{y,y} = 0\,, \tag{11}$$

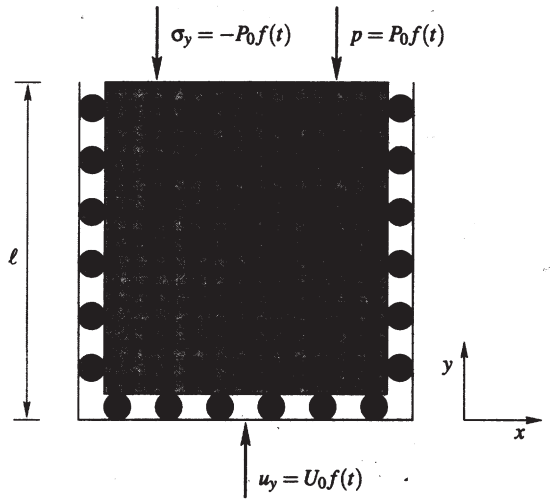


**Fig. 1.** One-dimensional column under dynamic loading

with the modulus $E = K + 4/3G$. The boundary conditions are

$$\begin{aligned} &\hat{u}_y(y=0) = U_0\,, \qquad \hat{q}_y(y=0) = 0 \qquad \text{and} \\ &\hat{\sigma}_y(y=\ell) = -P_0\,, \qquad \hat{p}(y=\ell) = P_0\,, \end{aligned} \tag{12}$$

where an impulse function for the temporal behavior $f(t) = \delta(t)$, with $\delta(t)$ denoting the Dirac distribution, is assumed, together with vanishing initial conditions. Each of the nonzero boundary conditions in (12) represents a different type of loading. Due to the neglected body forces this is a system of homogeneous ordinary differential equations with inhomogeneous boundary conditions. Such a system can be solved by the following exponential ansatz:

$$\hat{u}_y(y) = U e^{\lambda s y}\,, \qquad \hat{p}(y) = P e^{\lambda s y}\,. \tag{13}$$

Inserting the ansatz functions (13) in Eqs. (10) and (11) results in an Eigenvalue problem for $\lambda$

$$\begin{bmatrix} E\lambda^2 - (\varrho - \beta\varrho_f) & -(\alpha-\beta)\dfrac{\lambda}{s} \\ -s(\alpha-\beta)\lambda & \lambda^2 \dfrac{\beta}{\varrho_f} - \dfrac{\phi^2}{R} \end{bmatrix} \begin{bmatrix} U \\ P \end{bmatrix} = \mathbf{0}\,, \tag{14}$$

with the characteristic equation

$$\underbrace{E\frac{\beta}{\varrho_f}}_{A}\lambda^4 - \underbrace{\left(E\frac{\phi^2}{R} + (\varrho - \beta\varrho_f)\frac{\beta}{\varrho_f} + (\alpha-\beta)^2\right)}_{B}\lambda^2 + \underbrace{\frac{\phi^2(\varrho - \beta\varrho_f)}{R}}_{C} \stackrel{!}{=} 0\,. \tag{15}$$

The characteristic Eq. (15) has the four complex roots

$$\lambda_1 = -\lambda_3 = \sqrt{\frac{B + \sqrt{B^2 - 4AC}}{2A}} \qquad \lambda_2 = -\lambda_4 = \sqrt{\frac{B - \sqrt{B^2 - 4AC}}{2A}}\,. \tag{16}$$

This leads to the complete solution of the homogeneous problem

$$\hat{u}_y(y) = \sum_{i=1}^{4} U_i e^{\lambda_i s y}, \qquad \hat{p}(y) = \sum_{i=1}^{4} P_i e^{\lambda_i s y}. \tag{17}$$

The eight unknown constants $U_i$ and $P_i, i = 1, \ldots, 4$, can not be determined by the four boundary conditions (12) alone. Also none of the complex roots can be excluded due to physical reasons. But the Eigenvector of the system (14) gives the relation

$$P_i = \underbrace{\frac{E\lambda_i{}^2 - (\varrho - \beta\varrho_f)}{(\alpha - \beta)\lambda_i}}_{d_i} \cdot sU_i. \tag{18}$$

Finally, if the solution is inserted into the one-dimensional form of the constitutive Eq. (1.1)

$$\hat{\sigma}_y(s,y) = E\hat{u}_{y,y} - \alpha\hat{p} = E\sum_{i=1}^{4} \lambda_i s U_i e^{\lambda_i s y} - \alpha\hat{p}(s,y) \tag{19}$$

and the one-dimensional form of Darcy's law (6)

$$\begin{aligned}\hat{q}_y(s,y) &= -\frac{\beta}{s\varrho_f}\left(\hat{p}_{,y} + s^2\varrho_f\hat{u}_y\right) \\ &= -\frac{\beta E s}{\varrho_f(\alpha-\beta)}\sum_{i=1}^{4}\lambda_i{}^2 U_i e^{\lambda_i s y} + \beta s\left(\frac{\varrho - \alpha\varrho_f}{\varrho_f(\alpha-\beta)}\right)\hat{u}_y(s,y),\end{aligned} \tag{20}$$

the remaining four constants $U_i$ can be fit to the four boundary conditions. This leads to four equations for four unknowns which can be solved, preferably, with the aid of computer algebra.

Finally, the solutions for the displacements and the pore pressure is achieved by inserting these coefficients in the ansatz functions (17). As we are dealing with a linear problem the superposition principle is valid. Therefore, the solution can be divided in different load cases. The results for stress boundary conditions $\hat{u}_y(y=0) = 0, \hat{\sigma}(y=\ell) = -P_0$ and $\hat{p}(y=\ell) = 0$ are

$$\hat{u}_y = \frac{P_0}{E(d_1\lambda_2 - d_2\lambda_1)}\left[\frac{d_2(e^{-\lambda_1 s(\ell-y)} - e^{-\lambda_1 s(\ell+y)})}{s(1+e^{-2\lambda_1 s\ell})} - \frac{d_1(e^{-\lambda_2 s(\ell-y)} - e^{-\lambda_2 s(\ell+y)})}{s(1+e^{-2\lambda_2 s\ell})}\right], \tag{21}$$

$$\hat{p} = \frac{P_0 d_1 d_2}{E(d_1\lambda_2 - d_2\lambda_1)}\left[\frac{(e^{-\lambda_1 s(\ell-y)} + e^{-\lambda_1 s(\ell+y)})}{1+e^{-2\lambda_1 s\ell}} - \frac{(e^{-\lambda_2 s(\ell-y)} + e^{-\lambda_2 s(\ell+y)})}{1+e^{-2\lambda_2 s\ell}}\right]. \tag{22}$$

The corresponding stress and flux is calculated with the constitutive equation (19) and Darcy's law (20), respectively. The solutions corresponding to the other boundary conditions can be found in the Appendix B.

Note, due to the dependence of $\beta$ to the Laplace parameter $s$, the roots $\lambda_i$ and consequently $d_i$ are dependent of $s$. Therefore, an analytical inverse Laplace transform of the solutions above is in general not possible. However, if the damping due to the relative motion of the fluid and the solid is neglected, i.e., the permeability tends to infinity

$$\varkappa \to \infty \Rightarrow \beta \approx \frac{\phi^2\varrho_f}{\varrho_a + \phi\varrho_f}, \tag{23}$$

an analytical inverse Laplace transform can be found.

*Special case of* $\varkappa \to \infty$: Under this assumption $\beta$ and consequently $\lambda_i$ and $d_i$ are constant with respect to $s$. Then, in Eqs. (21) and (22) only the expressions with the exponential function are dependent on $s$. In the analysis of the corresponding elastic problem the same expressions appear. Following the procedure in [24], the series expansion

$$\frac{1}{1+e^{-2\lambda_i s\ell}} = \sum_{n=0}^{\infty} (-1)^{-n} e^{-2\ell n s\lambda_i} \tag{24}$$

gives

$$\frac{\left(e^{-\lambda_1 s(\ell-y)} - e^{-\lambda_1 s(\ell+y)}\right)}{s(1+e^{-2\lambda_i s\ell})} = \sum_{n=0}^{\infty} (-1)^{-n} \left(\frac{1}{s}\, e^{-\lambda_1 s\left(\ell(2n+1)-y\right)} - \frac{1}{s} e^{-\lambda_i s\left(\ell(2n+1)+y\right)}\right). \tag{25}$$

Now, an inverse Laplace transform is possible term by term of the series above. With the relations

$$\frac{1}{s}\, e^{-\lambda_i s\left(\ell(2n+1)-y\right)} \;\bullet\!\!-\!\!\circ\; H\Big(t-\lambda_i\big(\ell(2n+1)-y\big)\Big), \tag{26}$$

$$e^{-\lambda_i s\left(\ell(2n+1)-y\right)} \;\bullet\!\!-\!\!\circ\; \delta\Big(t-\lambda_i\big(\ell(2n+1)-y\big)\Big), \tag{27}$$

where $H(t)$ denotes the Heaviside step function and $\delta(t)$ the Dirac distribution, the inverse transform of (21) and (22) is given. Note that the Dirac distribution has to be defined as a generalized function. The response in time domain can be calculated with the convolution integral, e.g. for the displacements

$$u_y(t,y) = \int_0^t \mathscr{L}^{-1}\{\hat{u}_y(s,y)\}(\tau,y)\, f(t-\tau)\, d\tau, \tag{28}$$

where $\mathscr{L}^{-1}$ is the inverse Laplace transform operator. Assuming a Heaviside step function as temporal behavior of the load, i.e., $f(t) = H(t)$, the response in time domains is

$$\begin{aligned} u_y = \frac{P_0}{E(d_1\lambda_2 - d_2\lambda_1)} \sum_{n=0}^{\infty} (-1)^{-n} \Big\{ & d_2\Big[\Big(t-\lambda_1\big(\ell(2n+1)-y\big)\Big) H\Big(t-\lambda_1\big(\ell(2n+1)-y\big)\Big) \\ & - \Big(t-\lambda_1\big(\ell(2n+1)+y\big)\Big) H\Big(t-\lambda_1\big(\ell(2n+1)+y\big)\Big)\Big] \\ & - d_1\Big[\Big(t-\lambda_2\big(\ell(2n+1)-y\big)\Big) H\Big(t-\lambda_2\big(\ell(2n+1)-y\big)\Big) \\ & - \Big(t-\lambda_2\big(\ell(2n+1)+y\big)\Big) H\Big(t-\lambda_2\big(\ell(2n+1)+y\big)\Big)\Big]\Big\}; \end{aligned} \tag{29}$$

$$\begin{aligned} p = \frac{P_0 d_1 d_2}{E(d_1\lambda_2 - d_2\lambda_1)} \sum_{n=0}^{\infty} (-1)^{-n} \Big[ & H\Big(t-\lambda_1\big(\ell(2n+1)-y\big)\Big) + H\Big(t-\lambda_1\big(\ell(2n+1)+y\big)\Big) \\ & - \Big(H\Big(t-\lambda_2\big(\ell(2n+1)-y\big)\Big) - H\Big(t-\lambda_2\big(\ell(2n+1)+y\big)\Big)\Big)\Big]. \end{aligned} \tag{30}$$

In this solutions clearly two waves with the wave velocities $\lambda_i^{-1}$ are identified. With the same inverse transformations the time domain solutions of other boundary conditions are achieved.

*General case of arbitrary* $\varkappa$ : For an arbitrary value of $\varkappa$ a numerical inverse Laplace transformation is necessary. A number of methods are available in the literature, and the advantages

and disadvantages has been studied, e.g. in [19] or [25]. But, in this case here, where one function in the convolution integral (28) is only available in Laplace and the other function in time domain, it is preferable to take the "Convolution Quadrature Method" proposed by Lubich [15]. This method approximates the convolution integral (28) numerically by a quadrature formula

$$u_y(n\Delta t) = \sum_{k=0}^{n} \omega_{n-k}(\Delta t) f(k\Delta t)\,, \quad n = 0, 1, \ldots, N\,, \tag{31}$$

whose weights $\omega_{n-k}(\Delta t)$ are determined with the help of the Laplace transformed impulse response functions $\hat{u}_y(s, y)$ and a linear multistep method $\gamma(s)$

$$\omega_n(\Delta t) = \frac{\mathscr{R}^{-n}}{L} \sum_{\ell=0}^{L-1} \hat{u}_y\left(\frac{\gamma(\mathscr{R}e^{i\ell\frac{2\pi}{L}})}{\Delta t}\right) e^{-in\ell\frac{2\pi}{L}}\,. \tag{32}$$

Details of the used parameters can be found in the appendix A. In the following, the time dependent responses are evaluated with this method, choosing a backward differentiation formula of order 2 (BDF 2) as the underlying multistep method.

## 4 One-dimensional wave propagation

Wave propagation in the 1-d column sketched in Fig. 1 is studied in the following using the developed solutions. Three very different materials, a rock (Berea sandstone) [12], a soil (coarse sand) [26], and a sediment (mud) [27] are chosen to represent a wide range of porous materials. The material data are given in Table 1. In all calculations below it is assumed that the time history of the loading is a Heaviside step function.

First, to show the reliability of the proposed numerical algorithm (31), a comparison is made with Dubner and Abate's method [16]. For a finite column of length $\ell = 10$ m subject to a stress only loading of $\sigma_y(t, y = \ell) = -1$ N/m$^2$ and $p(t, y = \ell) = 0$ at the top, the displacements $u_y(t, y = \ell)$ at the top and the pressure $p(t, y = 0)$ at the bottom are plotted versus time in Fig. 2. For the convolution quadrature method, following suggestions concerning the choice of the parameters $L$ and $\mathscr{R}$, as reported in Appendix A, $\Delta t$ is the only parameter to be adjusted. To test the convergence, several $\Delta t$ values are chosen in the evaluation, with result plotted in dot and dash lines in Fig. 2.

Dubner and Abate's method, on the other hand, requires the empirical selection of two parameters, the real part of the Laplace variable $s$ denoted as $\alpha$, and the time period $T$. After a number of trial, the optimal values are chosen as $\alpha = 10$ for the displacement and $\alpha = 30$ for the pressure solution and $T = 0.8 * t_{\max}$, where $t_{\max}$ is the total observation time, for the soil case. The result is plotted in solid line in Fig. 2. For the two other cases, rock and sediment, multiple tries have failed to produce acceptable results. Hence only the soil case is compared.

**Table 1.** Material data of Berea sandstone, a soil, and a sediment

| | $K$ [N/m$^2$] | $G$ [N/m$^2$] | $\varrho$ [kg/m$^3$] | $\phi$ | $K_s$ [N/m$^2$] | $\varrho_f$ [kg/m$^3$] | $K_f$ [N/m$^2$] | $\varkappa$ [m$^4$/Ns] |
|---|---|---|---|---|---|---|---|---|
| rock | $8 \cdot 10^9$ | $6 \cdot 10^9$ | 2458 | 0.19 | $3.6 \cdot 10^{10}$ | 1000 | $3.3 \cdot 10^9$ | $1.9 \cdot 10^{-10}$ |
| soil | $2.1 \cdot 10^8$ | $9.8 \cdot 10^7$ | 1884 | 0.48 | $1.1 \cdot 10^{10}$ | 1000 | $3.3 \cdot 10^9$ | $3.55 \cdot 10^{-9}$ |
| sediment | $3.7 \cdot 10^7$ | $2.2 \cdot 10^7$ | 1396 | 0.76 | $3.6 \cdot 10^{10}$ | 1000 | $2.3 \cdot 10^9$ | $1 \cdot 10^{-8}$ |

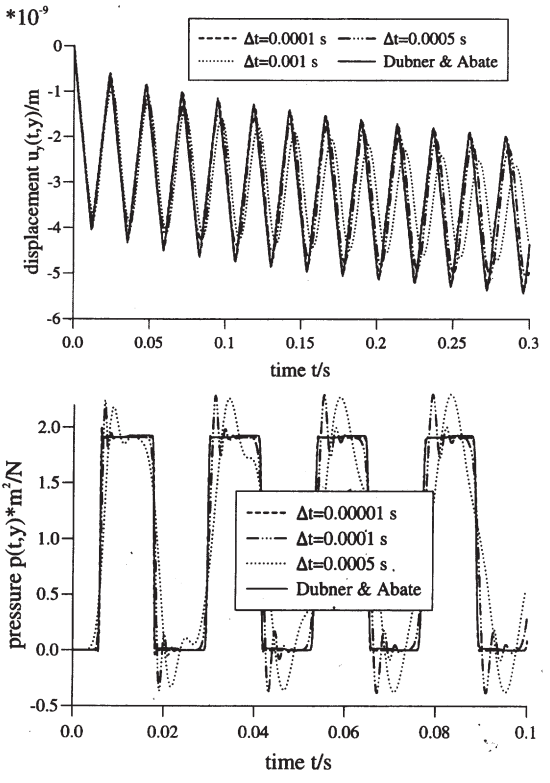


**Fig. 2.** Displacements $u_y\,(t, y = \ell)$ and the pressure $p\,(t, y = 0)$ versus time for different time step sizes $\Delta t$ compared with Dubner and Abate's inversion formula

In Fig. 2 it is observed that the accuracy of Lubich method is dependent on the time step size chosen in (31). If the time step $\Delta t$ is small enough, the result overlaps with the Dubner and Abate result for most part of the curve. The Lubich method solution, however, shows a slight overshooting at the wave front of the pressure, whereas the Dubner and Abate method had a slight difficulty in keeping constant values between two wave fronts. This first test has shown the reliability and robustness of the proposed method.

Before moving to the next problem, it is of interest to provide a physical interpretation of the results observed in Fig. 2. For the purpose of comparison, we first realize that for an elastic solution, the displacement at the top of column is given by triangular waves of constant amplitude that fluctuate around a constant mean value. In the poroelastic solution, we observe that the triangular wave form is largely preserved. The amplitude, however, diminishes with time due to fluid viscous dissipation, and will eventually go to zero. The mean value also drops with time. The mean fluctuation level is first around the static deformation value based on "undrained" material parameters, $u_{\text{static}} = 1.86 \cdot 10^{-9}$ m. As sufficient fluid has gained time to escape at the top of column, a "consolidation" is observed. The mean fluctuation level gradually settles into the "drained" static deformation value $u_{\text{static}} = 2.94 \cdot 10^{-8}$ m. As the soil column is being drained, the time for the wave to transverse the column will gradually increase.

We next examine the pressure response in Fig. 2. We observe the time of arrival of the first compressional wave at the bottom of the column. The amplitude is twice of that created by static Skempton effect due to the perfect reflection condition at the bottom. From the well

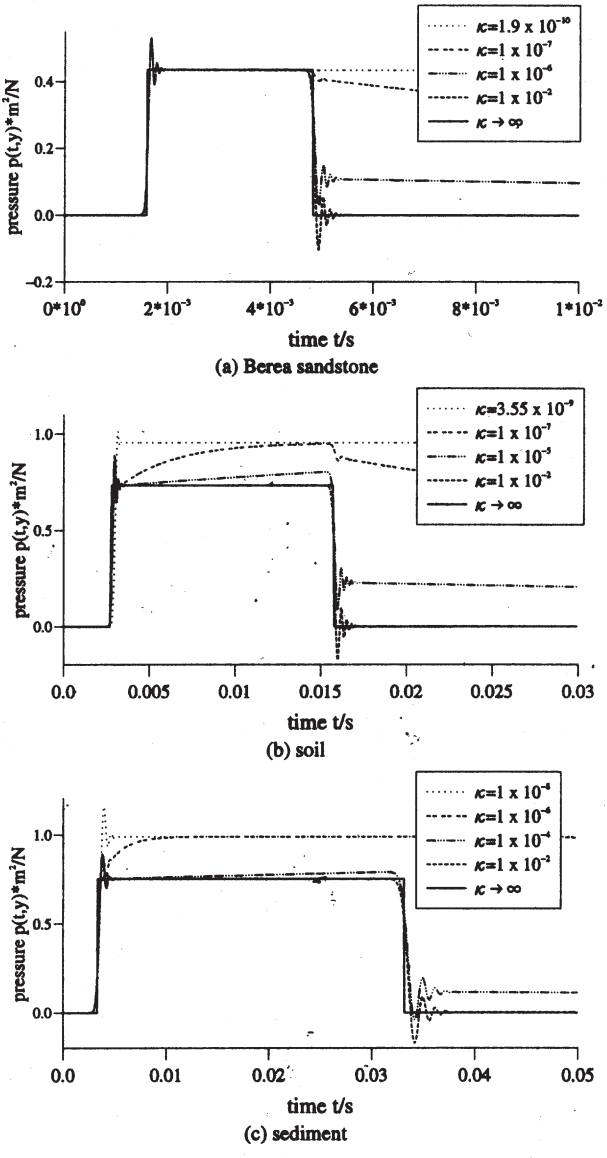


**Fig. 3.** Pressure $p\,(t, y = 995\,\mathrm{m})$ versus time for different values of $\varkappa$ compared with the analytical solution (30): infinite column

known one-dimensional wave propagation in a fixed-free end column, square waves are expected. If enough number of cycles are observed, the waves will eventually drop to zero due to dissipation.

In the above observed time range we did not detect the second compressional wave, known as the slow wave. This is attributed to the large ratio in wave speed such that the fast wave has the opportunity to transverse the column a number of times before the arrival of the slow wave at the bottom.

To unambiguously capture the slow wave, we examine in the next case an "infinite" column to avoid wave reflections. This is achieved by using a column length of $\ell = 1\,000$ m and a short observation time. In Fig. 3 we record the pressure, $p(t, y = 995$ m), five meters

behind the excitation point ($y = \ell = 1\,000$ m). Since this is the first time that we expect to observe such wave, it is compared with the exact time domain solution (30), shown as solid lines in Fig. 3 for the three materials, to gain confidence. To make the comparison, an arbitrarily large value, $\varkappa = 1 \cdot 10^{-2}$, is chosen in the Convolution Quadrature solution, with results plotted in dashed lines in Fig. 3. It is observed that, except for some fluctuations at wave fronts, which are generally unavoidable for all numerical inversion methods, the two solutions compare very well.

The phenomenon exhibited in Fig. 3 can be rationalized as follows. We first observe the arrival of the first wave at 5 m that causes the step jump. The second wave, arriving at a later time, is of negative amplitude and cancels exactly the first wave as indicated by the exact solution (30). The arrival time of the two waves is independent of $\varkappa$ as its limit has been taken.

To obtain and understand the solution of the realistic cases, we start to decrease $\varkappa$ values. Figure 3 shows a sequence of reduction that lead to the real values listed in Table 1. As $\varkappa$ decreases, we observe that both the amplitude and the arrival time of the waves are affected. The effect is strongest for the second wave. For some intermediate values of $\varkappa$, we observe that when the second wave arrives, its amplitude is diminished. Hence the pressure does not drop to zero at the passage of the wave front. We also observe that the second wave is dispersive as it does not arrive as a sharp front with constant value in some cases. Rather, the pressure continues to decline as seen in some curves.

As $\varkappa$ continues to derease, we find two effects. First, the wave speed of the second wave tends to zero as $\varkappa \to 0$. Second, the wave is rapidly dissipated such that it has no effect when it arrives at the 5 m point. In that case, we observe the clear arrival of the first wave only, and not the second wave. These observations are in accordance with the behavior of $\lambda_i$ with increasing and decreasing $\varkappa$.

Also, the comparison shows the different behavior of the three different materials on changing the permeability. For rock, the wave amplitude of the first wave is nearly independent from the permeability, contrary to the soil and the sediment.

If the same experiment is examined with a finite soil column, now $\ell = 10$ m, the reflections at both ends are visible (Fig. 4), and there are multiple arrivals. It is of interest to check the successive arrival time with theoretical result. However, the wave speed is not a constant when there exists dissipation. We can only use an estimate based on the special case of $\varkappa \to \infty$. In Table 2 wave speed for the special case is presented as $\lambda_i^{-1}$. The successive arrival times in the middle of the column (5 m) are shown as 1st, 2nd, etc. With these values, results for the undamped case can be interpreted. Referring to the lower diagram of Fig. 4, the pressure for the undamped case at 5 m is shown in solid line. At $t = 0.002\,8$ s, we observe the arrival of the fast wave. At $t = 0.008\,4$ s, the bottom reflected fast wave arrives. Next comes the top reflected fast wave at $t = 0.014\,0$ s. At $t = 0.015\,7$ s, the arrival of the slow wave negates the pressure. We can continue this to identify every arrival front.

The more interesting case is the real case with dissipation. Two $\varkappa$ values are used. For the intermediate value case, $\varkappa = 1 \cdot 10^{-5}$, we observe the significant modification of wave amplitude, especially after multiple reflections. The arrival time is roughly the same as the

**Table 2.** Arrival times of the two waves at $y = 5$ m in the finite column: material data of soil

| | $\lambda_i^{-1}$ | 1st | 2nd | 3rd | 4th | 5th | 6th |
|---|---|---|---|---|---|---|---|
| faster wave | 1 788 m/s | 0.002 8 s | 0.008 4 s | 0.014 0 s | 0.020 0 s | 0.025 2 s | 0.030 8 s |
| slow wave | 318 m/s | 0.015 7 s | 0.047 1 s | 0.078 6 s | 0.110 0 s | 0.141 5 s | 0.173 0 s |

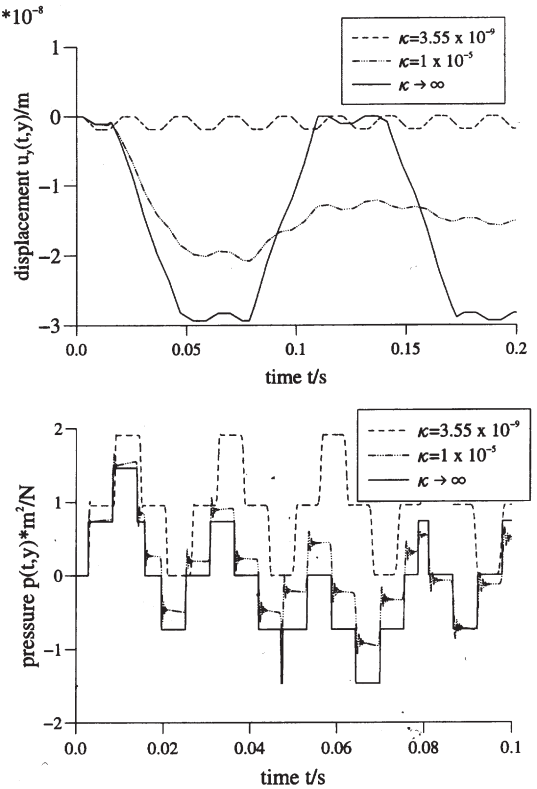


**Fig. 4.** Displacements $u_y\,(t, y = 5\,\mathrm{m})$ and the pressure $p\,(t, y = 5\,\mathrm{m})$ versus time for different values of $\varkappa$ compared with the analytical solution (30): finite soil column

undamped case. For the smallest permeability (actual value) case, the effect of slow wave is not visible. The wave profile is similar to the elastic case. However, if we closely track the arrival time and compare with the undamped case, we observe that the wave slows down after each reflection. This behavior is in accordance with the theory where $\lambda_i$ are functions of $s$, hence are time dependent, leading to time dependent wave velocities. In Fig. 4, we also observe that the sharp wave fronts are smoothed after each reflection, and that the wave amplitude diminishes with time.

The above description refers to pore pressure. The top diagram in Fig. 4 gives the displacement at $y = 5$ m. The solid line is the undamped case given by the exact solution. The dotted lines correspond to the two damped cases shown in the lower diagram.

Finally, the wave propagation with respect to both temporal and spatial variables is considered. In Fig. 5, the displacements $u_y(t, y)$ caused by a stress Heaviside step loading are depicted versus time and at the locations $y = 2.5\,\mathrm{m}, 5\,\mathrm{m}, 7.5\,\mathrm{m}, 10\,\mathrm{m}$. In this figure the Berea sandstone data are used with two different permeabilities to show the extreme case of vanishing damping compared to the realistic damping. The realistic case is dominated by the first compressional wave, as expected from the previous study. In the undamped case the faster wave is a kind of overtone to the slower wave.

In the next case, the boundary condition is changed to a pressure Heaviside step loading of 1 $\mathrm{N/m^2}$, while the total stress is zero. Although this case is physically unattainable, it is mathematically valid, and the result can be used in a superposition. If the top of column is

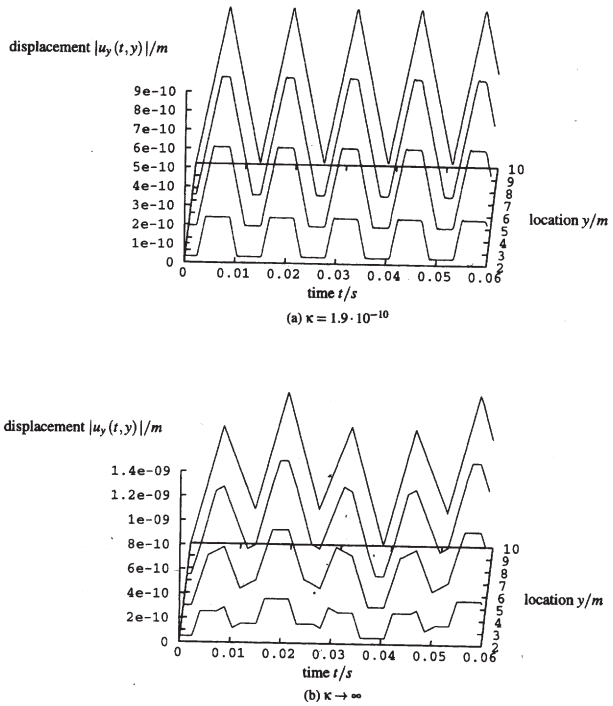


**Fig. 5.** Displacements $|u_y(t, y)|$ (absolute value) versus time at different locations $y$: finite rock column

exposed to a fluid and a step pressure rise is applied, the boundary condition consists of a stress part, and a pressure part, of which the current solution represents. We present this case to bring the relation of a pressure loading and the second wave into sharp focus.

In Fig. 6, the pressure $p(t, y)$ versus time at the locations $y = 0\,\text{m}, 2.5\,\text{m}, 5\,\text{m}, 7.5\,\text{m}$ is presented for Berea sandstone and the same permeabilities as before. The influence of $\varkappa$ is much stronger for pressure loading than for stress loading. In part (a), the small permeability case, the maximum amplitude is much smaller than that in part (b), and the wave propagates much faster. If part (b) is plotted in logarithmic scale, we can observe waves of very small amplitudes leading the large wave front shown in the figure. Hence the wave front observed in (b) is the slow wave with wave speed $\lambda_1^{-1} = 1\,037$ m/s. The first wave is not seen because it is too small. We recognize that the pressure boundary condition generates a second wave that travels undamped due to the high permeability condition. While the top of the column is total stress free, there is no compression generated at that point. A first wave is not generated at the boundary. As the second wave travels through the column, it emits the first wave of small amplitude, which outruns the second wave.

For the top figure (a), the small permeability case, we recognize the first wave by checking the approximate wave speed $\lambda_2^{-1} = 3\,137$ m/s. The first wave is observed only by plotting in the scale shown. We can use such small scale because unlike case (b), the second wave is all but vanished in amplitude when it reaches the observation points. Although the second wave survived only a short distance, the first wave that it generated is observed in this figure. The first wave does not have a sharp front because it is continuously emitted by the second wave.

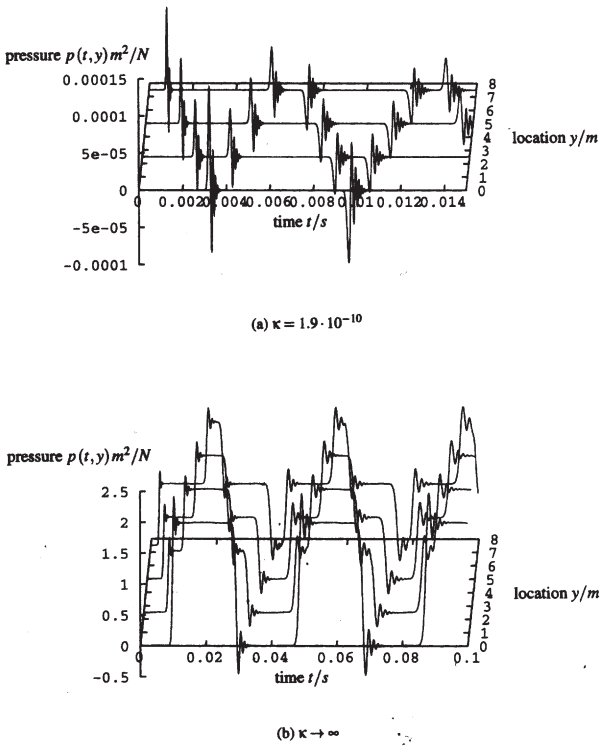


**Fig. 6.** Pressure $p(t, y)$ versus time at different locations $y$: finite rock column

Summarizing, the presented results clearly show two waves and their interplay under different loading and boundary conditions. But, for realistic values of permeability of the three used materials, the influence of the second compressional wave is small. Changing the permeability by using a different fluid, such as air, with low viscosity, especially in the case of pressure boundary conditions, a stronger influence of the second wave may be observed.

## 5 Conclusions

Based on Biot's theory, in the present paper an analytical solution in Laplace transform domain for a poroelastic 1-d column is deduced. The closed form exact solution in time domain is achieved for the special case of a permeability tending to infinity by an analytical inverse transformation. For the general case of an arbitrary permeability, i.e., damping due to the interaction of fluid and solid is taken into account, the inverse transformation can not be found analytically. Therefore, a numerical inverse Laplace transform is performed. Here, because only the convolution integral between the impulse response function and the boundary condition, but not the impulse response function itself, is needed, the so-called "Convolution Quadrature Method" proposed by Lubich is applied. This method approximates the convolution integral numerically using the Laplace transformed impulse response function and a linear multistep method.

Finally, the method is tested with three different material data, a rock, a soil, and a sediment. The proposed numerical method shows a robust behavior compared to the numerical inverse transformation method of Dubner and Abate. Two compressional waves are clearly identified in the limiting case of an infinite permeability. For some intermediate permeability cases the second wave is also present. However, for the actual permeabilities of the tested materials the effect of the second wave vanishes after a short distance. This paper does not test all practical materials, natural and man-made. There exist some materials, particularly those with small fluid viscosity and large medium permeability, in which the second wave effect can be significant.

## Appendix A

### Convolution Quadrature Method

The "Convolution Quadrature Method" developed by Lubich numerically approximates a convolution integral

$$y(t) = \int_0^t f(t-\tau)\, g(\tau)\, d\tau \quad \rightarrow \quad y(n\Delta t) = \sum_{k=0}^{n} \omega_{n-k}(\Delta t)\, g(k\Delta t)\,, \quad n = 0, 1, \ldots, N\,, \tag{33}$$

by a quadrature rule whose weights are determined by the Laplace transformed function $\hat{f}$ and a linear multistep method. This method was originally published in [15] and [28]. Application to the boundary element method may be found in [29]. Here, a brief overview of the method is given.

In formula (33) the time $t$ is divided in $N$ equal steps $\Delta t$. The weights $\omega_n(\Delta t)$ are the coefficients of the power series

$$\hat{f}\left(\frac{\gamma(z)}{\Delta t}\right) = \sum_{n=0}^{\infty} \omega_n(\Delta t)\, z^n\,, \tag{34}$$

with the complex variable $z$. The coefficients of a power series are usually calculated with Cauchy's integral formula. After a polar coordinate transformation, this integral is approximated by a trapezoidal rule with $L$ equal steps $2\pi/L$. This leads to

$$\omega_n(\Delta t) = \frac{1}{2\pi i} \int_{|z|=\mathscr{R}} \hat{f}\left(\frac{\gamma(z)}{\Delta t}\right) z^{-n-1}\, dz \approx \frac{\mathscr{R}^{-n}}{L} \sum_{\ell=0}^{L-1} \hat{f}\left(\frac{\gamma(\mathscr{R}e^{i\ell\frac{2\pi}{L}})}{\Delta t}\right) e^{-in\ell\frac{2\pi}{L}}\,, \tag{35}$$

where $\mathscr{R}$ is the radius of a circle in the domain of analyticity of $\hat{f}(z)$.

The function $\gamma(z)$ is the quotient of the characteristic polynomials of the underlying multistep method, e.g., for a BDF 2, $\gamma(z) = 3/2 - 2z + 1/2z^2$. The used linear multistep method must be $A(\alpha)$-stable and stable at infinity [28]. Experience shows that the BDF 2 is the best choice [30]. Therefore, it is used in all calculations in this paper.

If one assumes that the values of $\hat{f}(z)$ in (35) are computed with an error bounded by $\varepsilon$, then the choice $L = N$ and $\mathscr{R}^N = \sqrt{\varepsilon}$ yields an error in $\omega_n$ of size $\mathscr{O}(\sqrt{\varepsilon})$ [15]. Several tests conducted by the authors lead to the conclusion that the parameter $\varepsilon = 10^{-10}$ is the best choice for the kind of functions dealt with in this paper [20]. The assumption $L = N$ results in $N^2$ coefficients $\omega_n(\Delta t)$ to be calculated. Due to the exponential function at the end of formula (35) this can be done very fast using the technique of the Fast Fourier Transformation (FFT).

## Appendix B

### Analytical solutions in Laplace domain

The two solutions of Eqs. (10) and (11) in Laplace domain that are not presented in Sect. 3, corresponding to different boundary conditions, are presented below:

*pressure boundary conditions:*

$\hat{u}_y(y=0)=0\,,\hat{\sigma}_y(y=\ell)=0$ and $\hat{p}(y=\ell)=P_0$

$$\hat{u}_y=\frac{P_0}{Es(d_1\lambda_2-d_2\lambda_1)}\left[\frac{(E\lambda_2-\alpha d_2)\,(e^{-\lambda_1 s(\ell-y)}-e^{-\lambda_1 s(\ell+y)})}{1+e^{-2\lambda_1 s\ell}}\right.$$
$$\left.-\frac{(E\lambda_1-\alpha d_1)\,(e^{-\lambda_2 s(\ell-y)}-e^{-\lambda_2 s(\ell+y)})}{1+e^{-2\lambda_2 s\ell}}\right]; \tag{36}$$

$$\hat{p}=\frac{P_0}{E(d_1\lambda_2-d_2\lambda_1)}\left[\frac{d_1(E\lambda_2-\alpha d_2)\,(e^{-\lambda_1 s(\ell-y)}+e^{-\lambda_1 s(\ell+y)})}{1+e^{-2\lambda_1 s\ell}}\right.$$
$$\left.-\frac{d_2(E\lambda_1-\alpha d_1)\,(e^{-\lambda_2 s(\ell-y)}+e^{-\lambda_2 s(\ell+y)})}{1+e^{-2\lambda_2 s\ell}}\right]. \tag{37}$$

*displacement boundary conditions:*

$\hat{u}_y(y=0)=U_0\,,\hat{\sigma}_y(y=\ell)=0$ and $\hat{p}(y=\ell)=0$

$$\hat{u}_y=\frac{U_0}{E(\lambda_2{}^2-\lambda_1{}^2)}\left[\frac{(E\lambda_2{}^2+\alpha\varrho_f-\varrho)\,(e^{-\lambda_1 s(2\ell-y)}+e^{-\lambda_1 sy})}{1+e^{-2\lambda_1 s\ell}}\right.$$
$$\left.-\frac{(E\lambda_1{}^2+\alpha\varrho_f-\varrho)\,(e^{-\lambda_2 s(2\ell-y)}+e^{-\lambda_2 sy})}{1+e^{-2\lambda_2 s\ell}}\right]; \tag{38}$$

$$\hat{p}=\frac{U_0 s}{E(\lambda_2{}^2-\lambda_1{}^2)}\left[\frac{d_1(E\lambda_2{}^2+\alpha\varrho_f-\varrho)\,(e^{-\lambda_1 s(2\ell-y)}-e^{-\lambda_1 sy})}{1+e^{-2\lambda_1 s\ell}}\right.$$
$$\left.-\frac{d_2(E\lambda_1{}^2+\alpha\varrho_f-\varrho)\,(e^{-\lambda_2 s(2\ell-y)}-e^{-\lambda_2 sy})}{1+e^{-2\lambda_2 s\ell}}\right]. \tag{39}$$

The corresponding stresses and fluxes are easily calculated with the constitutive equation (19) and Darcy's law (20), respectively.

### Acknowledgement

Martin Schanz was supported by the German Research Foundation (DFG) under grant SCHA 527/4-1. The financial support is gratefully acknowledged.

## References


[1] Biot, M. A.: General theory of three-dimensional consolidation. Journal of Applied Physics **12,** 155–164 (1941).

[2] Biot, M. A.: Theory of elasticity and consolidation for a porous anisotropic solid. Journal of Applied Physics **26,** 182–185 (1955).

[3] Biot, M. A.: Theory of deformation of a porous viscoelastic anisotropic solid. Journal of Applied Physics **27** (5), 459–467 (1956).

[4] Biot, M. A.: Theory of propagation of elastic waves in a fluid-saturated porous solid I: Low-frequency range. Journal of the Acoustical Society of America **28** (2), 168–178 (1956).

[5] Biot, M. A.: Theory of propagation of elastic waves in a fluid-saturated porous solid II: Higher frequency range. Journal of the Acoustical Society of America **28** (2), 179–191 (1956).

[6] Plona, T. J.: Observation of a second bulk compressional wave in porous medium at ultrasonic frequencies. Applied Physics Letters **36** (4), 259–261 (1980).

[7] Ehlers, W.: Poröse Medien – ein kontinuumsmechanisches Modell auf der Basis der Mischungstheorie. Forschungsbericht aus dem Fachbereich Bauwesen 47, Universität – GH Essen 1989.

[8] Ehlers, W., Kubik, J.: On finite dynamic equations for fluid-saturated porous media. Acta Mechanica **105,** 101–117 (1994).

[9] Grag, S. K., Nafeh, A. H., Good, A. J.: Compressional waves in fluid-saturated elastic porous media. Journal of Applied Physics **45,** 1968–1974 (1974).

[10] Hong, S. J., Sandhu, R. S., Wolfe, W. E.: On Grag's solution of Biot's equations for wave propagation in a one-dimensional fluid-saturated elastic porous solid. International Journal for Numerical and Analytical Methods in Geomechanics **12,** 627–637 (1988).

[11] Hiremath, M. S., Sandhu, R. S., Morland, L. W., Wolfe, W. E.: Analysis of one-dimensional wave propagation in a fluid-saturated finite soil column. International Journal for Numerical and Analytical Methods in Geomechanics **12,** 121–139 (1988).

[12] Cheng, A. H.-D., Badmus, T., Beskos, D. E.: Integral equations for dynamic poroelasticity in frequency domain with BEM-solution. Journal of Engineering Mechanics ASCE **117** (5), 1136–1157 (1991).

[13] de Boer, R., Ehlers, W., Liu, Z.: One-dimensional transient wave propagation in fluid-saturated incompressible porous media. Archive of Applied Mechanics **63,** 59–72 (1993).

[14] Vgenopoulou, I., Beskos, D. E.: Dynamic behavior of saturated poroviscoelastic media. Acta Mechanica **95,** 185–195 (1992).

[15] Lubich, C.: Convolution quadrature and discretized operational calculus I. Numerische Mathematik **52,** 129–145 (1988).

[16] Dubner, H., Abate, J.: Numerical inversion of Laplace transforms by relating them to the finite Fourier cosine transform. Journal of the Association for Computing Machinery **15** (1), 115–123 (1968).

[17] Durbin, F.: Numerical inversion of Laplace transforms: an efficient improvement to Dubner and Abate's method. The Compute Journal **17** (4), 371–376 (1974).

[18] Crump, K. S.: Numerical inversion of Laplace transforms using a Fourier series approximation. Journal of the Association for Computing Machinery **23** (1), 89–96 (1976).

[19] Cheng, A. H.-D., Sidauruk, P., Abousleiman, Y.: Approximate inversion of the Laplace transform. The Mathematica Journal **4** (2), 76–82 (1994).

[20] Schanz, M., Antes, H.: Application of "Operational Quadrature Methods" in time domain boundary element methods. Meccanica **32** (3), 179–186 (1997).

[21] Detournay, E., Cheng, A. H.-D.: Fundamentals of Poroelasticity, vol. II. Comprehensive rock engineering: Principles, practice & projects, chap. 5, 113–171. Pergamon Press 1993.

[22] Bonnet, G., Auriault, J.-L.: Dynamics of saturated and deformable porous media: Homogenization theory and determination of the solid-liquid coupling coefficients. In Physics of Finely Divided Matter. (Boccara, N. and Daoud, M., eds.), 306–316. Berlin: Springer Verlag 1985.

[23] Bonnet, G.: Basic singular solutions for a poroelastic medium in the dynamic range. Journal of the Acoustical Society of America **82** (5), 1758–1762 (1987).

[24] Graff, K. F.: Wave motion in elastic solids. Oxford University Press 1975.

[25] Narayanan, G. V.. Beskos, D. E.: Numerical operational methods for time-dependent linear problems. International Journal for Numerical Methods in Engineering **18,** 1829–1854 (1982).

[26] Kim, Y. K., Kingsbury, H. B.: Dynamic characterization of poroelastic materials. Experimental Mechanics **19,** 252–258 (1979).
[27] Badiey, M., Cheng, A. H.-D., Mu, Y.: From geology to geoacoustics – evaluation of Biot-Stoll sound speed and attenuation for shallow water acoustics. Journal of the Acoustical Society of America **103** (1), 309–320 (1998).
[28] Lubich, C.: Convolution quadrature and discretized operational calculus II. Numerische Mathematik **52,** 413–425 (1988).
[29] Schanz, M., Antes, H.: A new visco- and elastodynamic time domain boundary element formulation. Computational Mechanics **20** (5), 452–459 (1997).
[30] Schanz, M.: A boundary element formulation in time domain for viscoelastic solids. Communications in Numerical Methods in Engineering **15,** 799–809 (1999).

**Authors' addresses:** Dr.-Ing. M. Schanz, Technical University Braunschweig, Institute of Applied Mechanics, P.O. Box 3329, D-38023 Braunschweig, Germany (E-mail: m.schanz@tu-bs.de); Prof. Alexander H.-D. Cheng, Department of Civil and Environmental Engineering, University of Delaware, Newark, Delaware 19716, USA (E-mail: cheng@ce.udel.edu)